VISUALISING AND ANALYSING PREDICTIONS OF ON-GROUND CASUALTY DISTRIBUTIONS

A. Herzog, T. Flohrer, H. Klinkrad

ESOC, Darmstadt, Germany
Email: {Alexandra.Herzog, Tim.Flohrer, Heiner.Kinkrad}@esa.int

ABSTRACT

For re-entry risk analysis the on-ground fragment swath of impacting debris objects is commonly approximated by a Gaussian distribution around the centre of impact window. However, the observed impact distributions show a positive skewness in along-track direction.

Here, we present enhanced tools for visualising simulated and observed on-ground distributions by connecting re-entry prediction and risk assessment tools to geographic information systems (GIS) with underlying models for spatial data, e.g., for the global population density. For a given re-entry prediction scenario these tools can provide, e.g., the probability for land impact, estimates for global casualty and fatality risks, and the corresponding risk figures for specific areas. The viability of these tools is demonstrated through processing a test set of historical re-entry events. In a second step, in order to improve the local casualty risk estimate, we analyse model candidates for an analytical approximation of skewed on-ground distributions. Suitable candidates are integrated into the visualisation tools for comparison with the classical Gaussian-based prediction, aiming to improve the quality in the estimation of the on-ground casualty risk.

Key words: re-entry; casualty analysis: on-ground-distribution.

1. INTRODUCTION

Since 1957 as of 2013 nearly 4950 launches have placed around 6710 satellites into orbit, together with rocket bodies, and mission-related objects into orbit. Slightly above 55 % of the latter objects are still in orbit [6]. Typically, one larger object re-enters into the deeper atmosphere every week. Re-entering space debris is a matter of large public interest, but also has political and legal aspects as it may impose a risk to humans on-ground. Predicting the re-entry of space objects requires a sound knowledge of the characteristics of the space object population and an adequate orbit determination and propagation capability that accounts for the relevant perturbing forces, especially of the air drag during the last phase of re-entering into the atmosphere. Modelling the air drag requires an effective model of the present atmospheric conditions beside the fragmentation state of the satellite and its current aerodynamic properties, hence air density distribution combined with prevailing wind fields. The analysis of past re-entry events has proven that the re-entry prediction capabilities with ESA's DISCOS [6] and the software tools in use at ESA's Space Debris Office (in particular the re-entry propagator FOCUS-2 [16]) enable an operational service for re-entry event prediction and risk assessment.

1.1. Aim of Research Project

In this research project we aimed to extend the operational software in two aspects: First, we headed for an extended visualisation of data output including a graphical environment for scalable two dimensional, optional three dimensional representations and animations.
Second, as observations suggested that the on-ground fragment distribution may not be adequately described by a Gaussian distribution [17] we tried to identify a selection of suitable candidates based on observed and simulated data sets for an extended development version of our re-entry software tools.

2. VISUALISATION OF GROUND TRACK DATA AND PREDICTIONS

2.1. Method: Integration of Geographic Information System

Software for re-entry prediction rely on an informative visualisation of the produced data output, i.e. the local probability of fragment impact depending on latitude, longitude and altitude. In its most plain form, this requires the access to global population density maps and plotting tools.
For improved visualising we created a python interface to the Geographic Resources Analysis Support System, abbreviated *GRASS*, a geographic information system

(GIS) of the Open Source Geospatial Foundation (OSGeo) [10]. *GRASS* provides access to basic and advanced GIS functionality (geographic projection, area calculation, etc) as well as access to visualisation modules for three-dimensional raster and point data by OpenGL integration via its plugin *NVIZ*.
Details on the implementation and compatibility of *GRASS* with other software libraries like R are discussed in [19]. For details on the programme package and its installation see the documentation in [10]. *GRASS* 6.4.2 was used in this project.

2.1.1. Programme organisation

GRASS is organised in *locations* and their subsidiary *mapsets*. A location contains at least the information on geospatial mapping as well as a main mapset *PERMANENT*, in which the central maps are stored that can be accessed from all further mapsets in the location.
For our project we defined the projection to geographic latitude-longitude covering the entire globe. *PERMANENT* contained the global raster maps we used for risk assessment, amongst these maps were a global population density map, a national identifier grid, and special supranational identifier grids (Europe, ESA-member states, etc), see figure 2 for examples. All raster maps in use were free-available raster-data sets, with a minimal resolution of $2.5'$. *Gridded Population of the World* [11] provided the global population density map in its data collection 'Population Density Grid', version 3 (1990, 1995, 2000), and the 'National Identifier Grid', version 3. The latter provided information on the location of nations, which formed the basis of the derived supranational identifier maps.
As *Gridded Population of the World* has a reduced geographical range of $\{-58.0°S; 85.0°N\}$, we derived binary maps based on the global maps of *Natural Earth* [18] for determining land coverage.
In the simplest case, the user of our extension module has to create a new mapset by calling a python script for each new re-entry event. So far we provided python interface scripts for output files of *FOCUS-2* and the *DRAMA* module *SESAM*. For a standard-call of the script the user has to pass location and name of the corresponding data files and to choose a name for the mapset to be created.
A call of the extension module generates vector maps of the ground track, i.e. the 2 σ swath across and along track, a vector map of the impact ellipsoid, and a three-dimensional vector map of the re-entry trajectory accessible via *NVIZ*. All maps are loaded in the created mapset as active maps to be accessible in the wxpython GUI of *GRASS*. In section 2.2 we provided a casualty risk vector map as an example.
If the user demands more accustomed maps, extensions and changes can be arranged in the sources of the development level as indicated in figure 1. Minor changes to the python script can be done solely in python, while development of runtime-demanding routines should include a precompilation with cython for performance reasons (translating e.g. python loops to c-loops [4]). However, performance of intersecting vector and raster data in *GRASS* itself is not affected significantly. For this reason we calculated areas and distances with the *C++*-library *GeoGraphic-Lib* [15] outside of *GRASS*. A simplified flow-chart of the implementation details is shown in figure 1.

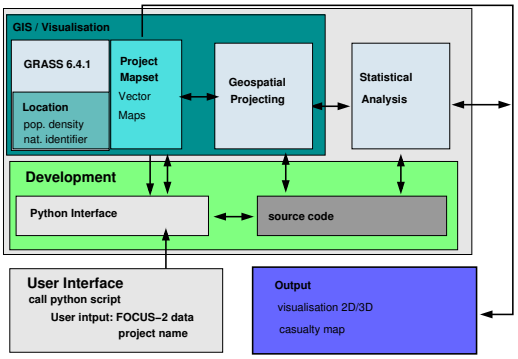

Figure 1. Simplified flow chart of programme suite implementation divided in development area and user space.

2.2. Visualisation Results

In this subsection we show an example map for risk visualisation. In figure 3 a casualty map was projected as a transparent overlay on the population density map. Casualty risk was colour-coded along and cross track. In this example, cross-track resolution was discretised in twelve risk levels as shown in figures 3 and 4. The user can adapt the desired discretisation individually.

3. FITTING OF ON-GROUND-DISTRIBUTIONS

Apart form the Columbia accident retrieval [1], detailed data sets of on-ground distribution of space debris are either rare, or are accessible only under restrictions, or are simply limited to a low number of fragments, e.g. in the case of the re-entry of Skylab [8, 23] 15 object positions were reported and in the case of Sputnik IV, 4 fragments were recorded with location [20]. Moreover, for these few objects, information on the fragments was also incomplete. In the above mentioned cases only the approximated location was recorded, while data on mass or ballistic coefficients β are not available (here β = mass/effective cross sectional area). These low numbers do not allow a reliable statistical analysis, beyond the calculation of a median and a measure of dispersion in the best case. Estimates of skewness or kurtosis of a distribution need at least a sample size of thirty [9, 5].

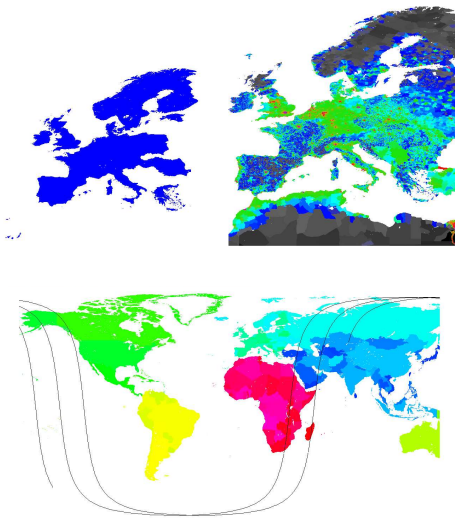

Figure 2. Example mapset: (top) maps from mapset PERMANENT, left binary map of Europe, right population density map; (bottom): national identifier grid together with overlay of a re-entry trajectory vector map in black from RENFOT; global maps based on [11].

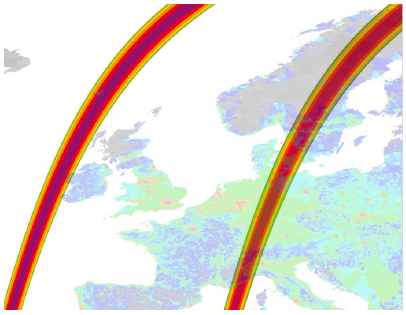

Figure 3. Casualty probability as determined by FOCUS-2 projected on population density map for the test scenario. The image shows the enlarged tracks of the last two revolutions before the predicted impact. Colour coding of fatality risk ranges from grey over yellow to dark magenta for highest encountered risk. Population density appears as grey below one inhabitant per square kilometre; population density increasing over blue, green, yellow, orange, red to magenta.

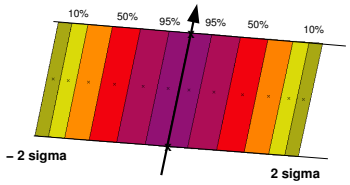

Figure 4. Details on cross-track probability distribution: each field represents a certain threshold of the highest value at along-track position ranging from 10 - 95% of the maximum value.

Figure 5. Distribution of recorded Skylab fragments: reported location of fragments plotted in red were projected over the population density map of Australia. The first red dot from the left marks the assumed position of solar panel debris.[8, 23, 11]

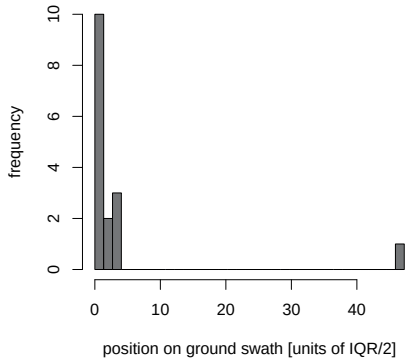

Figure 6. Distribution of Skylab retrieved fragments on land: histogram of along-track fragment distribution as reported in [8, 23].

3.1. Data sets for candidate evaluation

3.1.1. Observed re-entries

As data sets for observed re-entry events are rare, we restrict ourselves to the re-entry of Skylab in 1979 [8, 23]. The individual fragment locations and a histogram of fragment positioning along track are shown in figures 5 and 6. This small data set already reveals a characteristic of on-ground fragment distributions: The distribution was strongly skewed. Objects with high area to mass ratio, hence small ballistic coefficients, mark the beginning of the footprint due to aerodynamic reasons [2].

3.1.2. Simulated re-entries

For the simulation of a re-entering generic satellite we used *RENFOT* [3] a new developed software based on the modules *SESAM* and *ESESAM* of *DRAMA* [7] with a de-

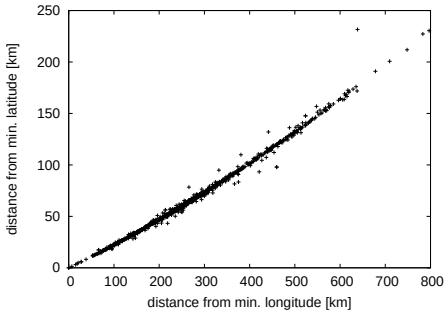

Figure 7. Simulated fragment distribution with RENFOT [3].

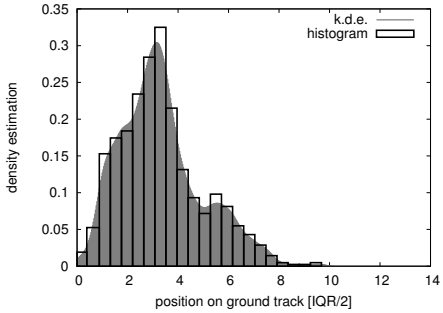

Figure 8. Density estimates for fitting: the origin of the density distribution estimate was shifted to the first bin to ensure non-negative x-range, there the fragments with lowest mass to area ratio are located. The graphic shows the kernel density estimate of the probability density function (p.d.f) of the distribution (Gaussian kernel) with overlay of a classic histogram based on the same binwidth; the half of the inter-quartile range (an estimate of the dispersion) is used as unit scale. Calculation was performed with R-package 'kernSmooth'. This estimate is used for fitting model candidates.

fault break-up simulation at an altitude of 95 km for solar panels and 78 km for the main body. For aerodynamic simulations randomly tumbling objects are assumed. A cross-track dispersion was induced here by the break-up process.
In this way the impact positions of several thousand individual fragments can be determined together with their physical properties as ballistic coefficients. Based on these simulations we tried to identify a suitable estimate of the density distribution. For histogram representation of the distribution we determined the binwidth using the algorithm proposed by Wand in [24] based on kernel density estimation. The resulting estimated distribution is shown in figure 8 both as histogram and kernel density estimation. In the next subsection we present the results of a simulated re-entry. In figure 9 we show a plot of the ballistic coefficients of the fragments to illustrate the orientation of our histogram data with respect to the footprint.

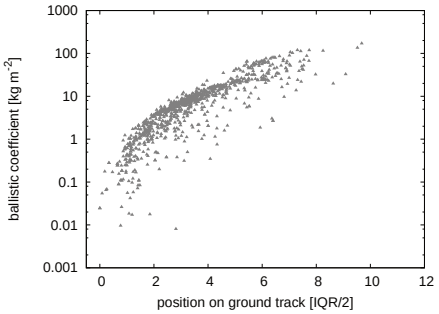

Figure 9. Ballistic coefficients of the fragment distribution in km-grid of the RENFOT/SESAM simulation.

Table 1. Selected measures for deviation from the Gaussian assumption of on-ground fragment distribution. Values shown for data from Skylab and a RENFOT simulation.

test data set	**mean-median**	**skewness**	**kurtosis**
Skylab	2.8	n.a. (2.5)	n.a. (11.1)
Sim_DRAMA	0.2	0.7	3.3

3.1.3. Qualitative characteristics of on-ground-distribution

The following characteristics were derived from the observed and simulated on-ground fragment distributions: the distribution of fragments is skewed with the fragments of small area to mass ratios or high ballistic coefficients in the right tail in along-track direction, as illustrated in table 1 for a *RENFOT* simulated distribution. Fragments with high ballistic coefficients typically include those of a high mass and therefore a high fatality index, see figure 10 for the product of fatality index and combined cross section, a quantity that may serve as a measure for fragment fatality. Hence, fragments with a high fatality can be expected in this tail of the distribution.

Please note, for the Skylab data we did not take into account the projected footprint position of debris on the ocean; only actually retrieved fragments were used for calculation [23, 20].
Positive difference of mean and median as well as the positive skewness are measures for a positively-skewed distribution. The observed kurtosis greater than 3 indicated heavier tails than a Gaussian distribution [9]. Skewness and kurtosis of the Skylab data set were not applicable (n.a.) as stated before.

In the following section we selected suitable model candidates.

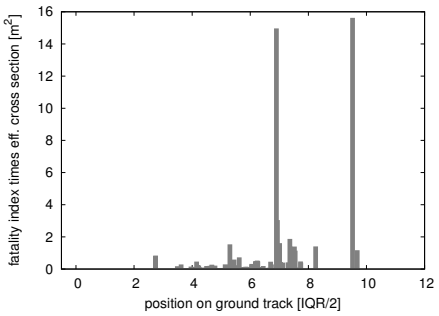

Figure 10. Estimating the fatality risk of fragments: fatality index times cross section area was plotted. Fragments with a high fatality risk were present in the tail. (data from RENFOT simulation).

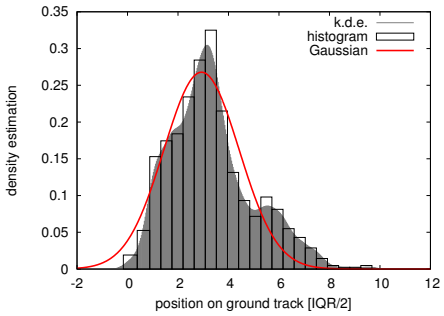

Figure 11. Fitted Gaussian distribution.

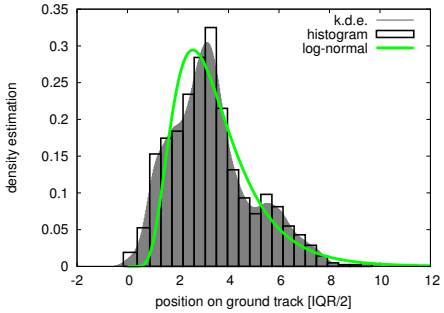

Figure 12. Fitted Log-Normal distribution.

3.2. Statistical analysis

For analysis of the on-ground distribution we followed these individual steps:

(i) projection of latitude-longitude on-ground distribution on the Cartesian-km-grid,

(ii) fitting of on-ground distribution with a polynomial up to order three,

(iii) setting of position of first bin of histogram as origin,

(iv) determining five-number summary (quartiles, interquartile range, and range) and first central moments (i.e. expectation value, variance, skewness, kurtosis) of mass and fragment distribution, and

(v) fitting of distribution candidates to the histogram data (initial values for model parameters were set to match moments or five-number summary of distribution).

Statistical analysis of the on-ground distribution was performed with the software package *R* [12]. *R* offers a plugin for *GRASS* called *spgrass6*.

3.2.1. Test candidates for on-ground distribution of fragments

In order to identify suitable candidates, we defined the following selection criteria based on the data properties described in the previous sections: The distribution should have (i) support on the semi-infinite interval $[0, \infty)$, should be (ii) positively skewed and ideally should also be (iii) analytically differentiable, have (iv) analytical moments, and a (v) low number of parameters.

The first test candidates included these distribution, which have a maximum number of two parameters:

$$\text{Gaussian} \qquad f(x;\sigma,\mu) = (\sigma\sqrt{2\pi})^{-1} e^{-\frac{(x-\mu)^2}{2\sigma^2}} \tag{1}$$

$$\text{Log-normal} \qquad f(x;\sigma,\mu) = (\sigma\sqrt{2\pi})^{-1}\, e^{-\frac{(\ln x-\mu)^2}{2\sigma^2}}, \quad x \geq 0; \sigma \geq 0; \mu \in \mathbb{R} \tag{2}$$

$$\text{Raygleigh} \qquad f(x;\sigma) = x\sigma^{-2} e^{-x^2/2\sigma^2}, \quad x \geq 0; \sigma > 0 \tag{3}$$

$$\text{Gamma} \qquad f(x;k,\theta) = \theta^{-k}\Gamma(k)^{-1} x^{k-1} e^{-\frac{x}{\theta}}, \quad x > 0;\ k,\theta > 0. \tag{4}$$

Parameters of the distributions to fit were estimated using Huber's-M-estimator [13].

3.3. Fitting Results

The result of the parameter fitting of the test candidates are presented in figures 11 to 14.

3.4. Goodness of fit: model discrimination

For evaluating goodness of fit we performed a sequence of statistical tests, including the Shapiro-Wilk test of normality, Kolomogorov-Smirnov, and the Anderson-Darling test [5, 21, 22]. These broad spectrum tests tend to accept the null hypothesis (a match of the proposed

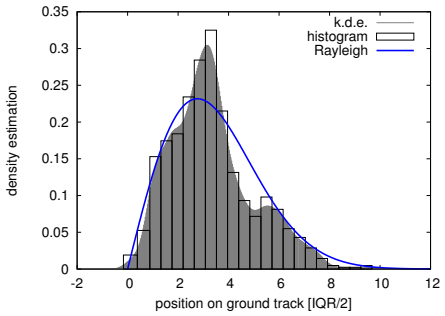

Figure 13. Fitted Rayleigh distribution.

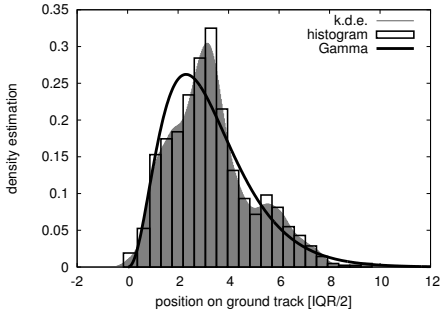

Figure 14. Fitted Gamma distribution.

distribution with the histogram) for similar distributions - a result to be expected for a low number of data points as described by Breiman in [5]. Therefore, we followed Breiman's procedure to locate significant deviations from the proposed distributions, as visualised by the residuals, which are plotted in figures 15 –18. We aimed for a good representation of the tails of the on-ground distribution as the tail-region corresponds to the region of smallest area to mass ratio, hence approximately to the region of highest kinetic energy of the fragments. In that respect the residuals of Rayleigh, log-normal and gamma distribution were much more promising compared to the Gaussian distribution, while fitting of the central part of the distribution was performed slightly better by the Gaussian. The parameter sets of log-normal, Rayleigh and Gaussian distribution had to be extended by an additional scaling parameter of total height for acceptable fitting results, while the gamma distribution did not depend on that.

Summarising, none of the here presented distribution candidates demonstrated a remarkable quality of matching the observed and simulated distributions. The gamma distribution generated the best trade-off in fitting the central parts and the tails of the distribution for our test scenarios in combination with residuals that showed almost an equal ratio of components above and below zero.

These preliminary results suggested that an on-ground distribution generated by a complex fragment distribution and an interaction with the atmospheric environment may be beyond the scope of a simple unimodal distribution. We considered this in more detail in the next section.

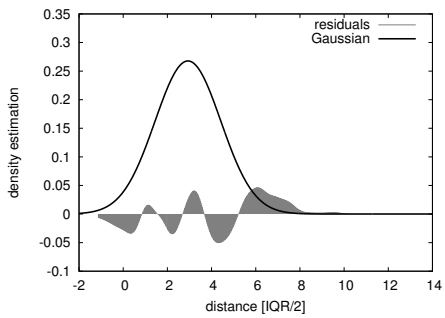

Figure 15. Residuals of Gaussian fit; best fit of central region.

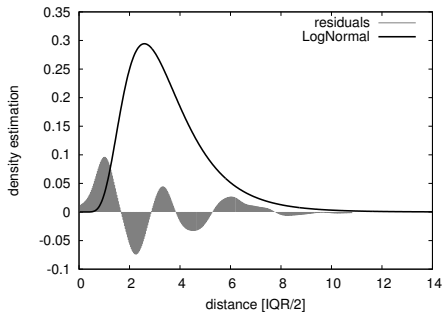

Figure 16. Residuals of Log-normal fit; residuals show an expressed dependency on location.

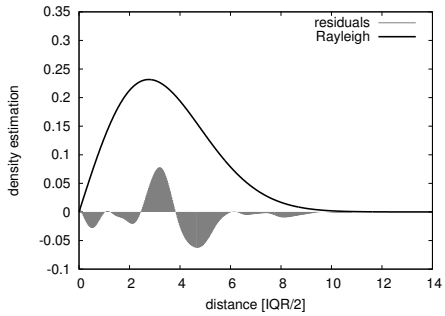

Figure 17. Residuals of Rayleigh fit; best fit of steep leading tail and tail but problems around maximum.

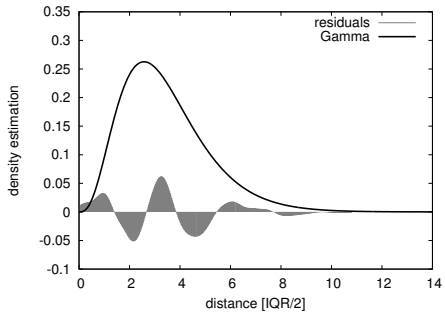

Figure 18. Residuals of Gamma fit; almost same amount of residuals above and below zero.

3.5. Theoretical considerations

In the current section, we related our empirical considerations of the previous section to a theoretical concept to estimate the on-ground fragment distribution.
We illustrated this concept in a simple example: As a start, we hypothesised an exponential atmosphere. We presumed that the main source of fragment spread was due to fluctuations (e.g. solar flux, wind fields) of air density and could be expressed in a random distribution of the scale height H_0. The fluctuations H' of the scale height should follow a Gaussian distribution $G(H')$ with zero mean. With these basic assumptions the probability density distribution (p.d.f) of the air density can be shown to be log-normally distributed up to first order:

$$\begin{aligned} f_{atmo}(\rho) &= \rho_0 \cdot \exp\left(-z/(H_0 + G(H'))\right) \\ &\doteq \rho_0 \cdot \exp\left(-z/H_0\right) \exp\left(z/H_0^2 \cdot G(H')\right) \\ &\doteq \rho(z) \exp\left(a \cdot G(H')\right), \end{aligned} \quad (5)$$

with $a := z/H_0^2$ and $\rho(z) := \rho_0 \cdot \exp\left(-z/H_0\right)$ as the undisturbed exponential density relation and with ρ_0 as the air density at sea level under standard conditions. Transforming the random variable via $exp(\cdot)$ and applying the chain rule led to

$$\begin{aligned} f_{atmo}(\rho) &\doteq \rho(z) \cdot G\left(ln(H')/a\right) \cdot \left| \frac{dH'}{d(\exp\left(aG(H')\right)} \right| \\ &\doteq \rho(z) \cdot G\left(ln(H')/a\right) \cdot \left|1/(aH')\right| \end{aligned} \quad (6)$$

The density is contained as a multiplicative factor in the equations of motion, here written for the along track acceleration component of a non-tumbling spheric body subject only to air drag

$$\begin{aligned} \frac{d^2}{dt} x &= f_{atmo}(\rho(z(t))) \cdot c_D/(2 \cdot \beta) \cdot v_x^2(t) \\ &= G\left(ln(H')/a\right) \cdot |1/(aH')| \cdot a_{det}(x, t; \beta) \end{aligned} \quad (7)$$

with β as the ballistic coefficient and c_D as the drag coefficient. Therefore, solving the system of differential equations for the trajectory we could conclude that the on-ground distribution for a fixed ballistic coefficient should also produce a log-normal distribution on ground around location x

$$f_{atmo}^{gr}(x) = G\left(ln(H')/a\right) \cdot \left|1/(aH')\right| \cdot t_{det}(x, \beta), \quad (8)$$

with $t_{det}(x, \beta)$ as the deterministic trajectory for a fixed ballistic coefficient β. Moreover, we know that a certain ballistic coefficient would lead to a certain deterministic impact location x' if and only if no spread occurred due to atmospheric influences. Yet, in a fragmentation event also a distribution of fragments of varying ballistic coefficients f_β is created.
As the number of small particles with a high area to mass ratio (i.e. low ballistic coefficient) can be expected to be much larger than particles with higher ballistic coeffcients we assumed an effective exponential on-ground distribution of fragments of a certain ballistic coefficient $f_\beta^{gr}(x')$ at location x':

$$f_\beta^{gr}(x') := \begin{cases} N_0^\beta \exp\left((x' - x_0)/D_0\right), & \text{if } x' < x_0 \\ 0 & \text{if } x' \geq x_0 \end{cases}$$

with N_0^β as largest number of fragments of the cut-off ballistic coefficient of the set, and D_0 as distance scale; x_0 implies the along-track position of the smallest encountered ballistic coefficient. This distribution would represent the expected on-ground distribution without any atmospheric disturbances.
Hence, the final distribution of the on-ground fragments should result from the effective interaction of by both distributions:

$$f_{sum}^{gr}(x) = \int_{-\infty}^{+\infty} f_{atmo}^{gr}(x; x = x') \cdot f_\beta^{gr}(x') dx'. \quad (9)$$

Other fluctuation terms such as continuing fragmentation were neglected.

The distribution f_{atmo}^{gr} maps a fragment that would be mapped deterministically[2] at position x with a probability of $f_{atmo}^{gr}(x', x)dx'$ to a position in the interval dx around x. The influence of the effective atmospheric density function can now be interpreted as a 'point spread function' (see for example the textbook [14]) of the otherwise deterministic re-entry trajectory. In a more general case, the effective atmospheric spread function would include locally varying parameters like wind fields.
Combining these assumptions the on-ground distribution $f_{sum}^{gr}(x)$ can be interpreted as a convolution of the distribution of the deterministic ballistic coefficient distribution and the atmospheric spread distribution. Fourier transformed this leads to a simple multiplication:

$$FT(f_{sum}^{gr}(x)) = FT(f_\beta^{gr}(x)) \cdot FT(f_{atmo}^{gr}(x)) \quad (10)$$

$$FT(f_{atmo}^{gr}(x)) = FT(f_{sum}^{gr}(x))/FT(f_\beta^{gr}(x)) \quad (11)$$

In the presented example we made a forward calculation for a given f_{atmo}^{gr} and determined the resulting on-ground distribution $f_{sum}^{gr}(x)$. However, we could also aim for the inverse: It is possible to determine $f_{atmo}^{gr}(x)$ for given distributions of the ballistic coefficient f_β^{gr} and the observed on-ground distribution of fragments $f_{sum}^{gr}(x)$ by inverse convolution.
Performing Monte-Carlo simulations under varying specific atmospheric conditions as e.g. stratospheric wind fields we could produce on-ground distributions for these situations and for arbitrary distributions of the ballistic coefficient. As simulated on-ground distribution and ballistic coefficient would be known, atmospheric spread could be determined. We now aim for identifying atmospheric point spread functions $f_{atmo}(x; p)$ for a set of varying parameters i.e. conditions based on Monte-Carlo simulations or in other words a classification of typical atmospheric point spread or transfer functions.

4. CONCLUSIONS AND OUTLOOK

With the interface to *GRASS*, we provided an extension module for enhanced visualisation of the output of *FOCUS-2* and *DRAMA/RENFOT* in 2 and 3 dimensions. Furthermore, our investigations of possible candidates for on-ground fragment distributions lead to identifying the

gamma distribution as promising for fitting both broad spectrum and tails; we plan to examine these results in further simulations under varying conditions. Our first steps towards a description of the atmospheric effects as a point spread function will be continued.

ACKNOWLEDGMENTS

The authors gratefully acknowledge financial support by an ESA internal research grant. Special thanks go to Benjamin Bastida Virgili, Quirin Funke and Stijn Lemmens for their support in preparing and conducting this project.

REFERENCES

1. Ailor, W. and Wilde, P. (2010). Requirements for warning aircraft of reentering debris, *AIAA Aircraft protecion standards*

2. Allen, H. J. and Eggers, A. J. (1953). A study of the motion and aerodynamic heating of ballastic missiles entering the earth's atmosphere at high supersonic speeds. Report 1381, *Ames Aeronautical Laboratory Moffet Field*, Calif.

3. Bastida Virgili, B., Krag, H. Lips, T. De Pasquale, E.(2013) Simulation of the ATV re-entry observations. *Proceedings of the Fourth IAASS Conference 'Making Safety Matter'* Huntsville, Alabama, USA, September 2010

4. Behnel, S., Bradshaw, R., Citro, C., Dalcin, L., Seljebotn, D. S., Smith, K. (2011) Cython: The best of both worlds. *IEEE Proceeding: Computing Science and Engineering*, **13** (2), 31–39

5. Breiman, L. (1973) *Statistics: With a view towards Applications*, Houghton Mifflin Company, Boston

6. Flohrer, T., Lemmens, S., Bastida-Virgili, B., Krag, H., Klinkrad, H., Parilla, E., Sanchez, N., Pina Caballero, F. (2013) DISCOS - current status and future developments. *Proceedings of the 6th European Conference on Space Debris* Darmstadt, 22-25 April 2013

7. Martin, C., Cheese, J., Sanchez-Ortiz, N., Bunte, K., Klinkrad, H. Lips, T., Fritsche, B., Koppenwallner, G. (2005) *Debris Risk Assessment and Mitigation Analysis (DRAMA) Tool*, ESA/ESOC Final Report of Contract No. 16966/02/D/HK

8. Dreher, P. E., Little R. P., Wittenstein, G. (1980) *Skylab orbital lifetime, prediction and decay analysis*, NASA Technical Memorandum, 78308

9. Dunlop, D., Tamhane, A. C. (2000) *Statistics and Data Analysis*, Prentice Hall

10. GRASS Development Team. (2012) Geographic Resources Analysis Support System (GRASS) Programmer's Manual. Open Source Geospatial Foundation. Electronic document: http://grass.osgeo.org/programming6/

11. Center for International Earth Science Information Network (CIESIN)/Columbia University, United Nations Food and Agriculture Programme (FAO), and Centro Internacional de Agricultura Tropical (CIAT). (2005). *Gridded Population of the World, Version 3 (GPWv3): Population Count Grid*. Palisades, NY: NASA Socioeconomic Data and Applications Center (SEDAC). *http://sedac.ciesin.columbia.edu/data/set/gpw-v3-population-count*. Accessed 30 November 2012

12. Hornik, K., (2013) *The R FAQ*, url http://CRAN.R-project.org/doc/FAQ/R-FAQ.html

13. Huber, P. J., (1964) Robust Estimation of a Location Parameter. *The Annals of Mathematical Statistics*. **35** (1),73–101

14. Jähne, B., (2005) *Digital Image Processing*. Springer, Heidelberg

15. Karney, C. F. F., (2013) Algorithms for geodesics. *Journal of Geodesy*, **87** (1), 43–55

16. Gonzales-Laguna, E., Klinkrad, H.(1989) *FOCUS-1 Fast Orbit Computation Utility Software*. MAS, WP 305, ESA/ESOC Darmstadt, Germany September 1998

17. Klinkrad, H. (2006) *Space Debris: Models and Risk Analysis*. Springer

18. Natural Earth. Free vector and raster map data *www.naturalearthdata.com* Accessed 17 December 2012

19. Neteler, M. Bowman, M. H., Landa, M., Metz, M. (2012) GRASS-GIS: A multi-purpose open source GIS *Environmental Modelling & Software*, **31**, 124–130

20. Neuenfeld, B. D. and Henderson, W. K. (1993) *A Survey of uncontrolled satellite re-entry and impact prediction*. Master Thesis, Naval Postgradual School, California; online: *http://oai.dtic.mil/oai/oai?verb=getRecord&metadataPrefix=html&identifier=ADA274903*

21. Royston, J. P. (1982) An Extension of Shapiro and Wilk's W Test for Normality to Large Samples. *Journal of the Royal Statistical Society. Series C (Applied Statistics)*, **31**(2), 115–12

22. Shapiro, S. S., Wilk, M. B. (1965) An analysis of variance test for normality. *Biometrika*, **52**(3-4), 591–611

23. Varnado, C. L. (1980) *Skylab Re-entry and Impact Footprint Reconstruction* NASA Report, George C. Marshall Space Flight Center, EL25-006

24. Wand, M. P. (1996) Data-Based Choice of Histogram Bin Width. *The American Statistician*, **51**, 59–64